


# Large Eddy Simulation Exploration of Passive Flow Control Around an Ahmed Body

"J. Fluids Eng 136(12), 121103 (Sep 10, 2014) (10 pages) doi:10.1115/1.4027221"

# LES exploration of passive flow control around an Ahmed body

**Siniša Krajnović**
Division of Fluid Dynamics
Department of Applied Mechanics
Chalmers University of Technology
SE-41296, Gothenburg, Sweden
Email: sinisa@chalmers.se

## ABSTRACT

*Large eddy simulations are used to study passive flow control for drag reduction in a simplified ground vehicle. Add on devices in the form of short cylinders are used for the formation of streaks in the streamwise direction that lead to the separation delay. The results of the present numerical simulations are compared with the experimental data and show good agreement. The two-stage flow control mechanism is analyzed from the LES results. It was found to be in agreement with the previous experimental observations that the counter-rotating vortices behind the impinging devices influence the separation only indirectly through the longitudinal vortices further downstream.*

**Nomenclature**

$H$ Height of the vehicle model..
$\lambda_z$ Spanwise spacing of the cylinder.
$d$ Diameter of the cylinder.
$k$ Height of the cylinder.
$\hat{A}_{st}$ Amplitude of the streak..
$q$ Adjoint pressure.
$C_p$ Surface pressure coefficient.
$U_e$ Inlet velocity.
$\overline{u}$ Resolved velocity in x direction.
$y^+$ Dimensionless wall distance.

## INTRODUCTION

Flow control strategies that aim to reduce drag in ground vehicles range from passive techniques using vortex generators, cavities and splitter plates to active techniques using either blowing or suction or a combination of both. There are also other more exotic techniques where a reduction in drag is achieved using momentum injection or plasma actuators. Several of the techques suggested have shown good results for generic vehicle bodies. It is important to note that most trials with flow control devices have been performed at low or moderate Reynolds numbers and at controlled conditions of a wind tunnel without any atmospheric turbulence, crosswinds or interaction with other vehicles. The fact is that, despite all the research so far, none of the proposed flow control techniques has proven to perform well at the operational flow conditions of real vehicles. Almost all proposed control strategies have serious drawbacks related to either practical application of the control, safety issues and law regulations or dependency on the flow conditions. The positive effect of most flow control strategies is strongly dependent on keeping constant flow conditions around vehicles for which flow control is designed. At flow conditions different from the optimal, the flow control often becomes an additional contributor that increases the total drag. The long term solution for an efficient flow control strategy is in closed-loop active flow control. There are several challenges in achieving a closed-loop control strategy as the actuation has to adjust to the flow conditions. This requires not only a better understanding of the flow around vehicles but also greater knowledge of the interaction of actuation with the flow and finding a good measure of the flow that can be used as an input for flow control in order to provide an optimal actuation. This research is ongoing, and the present paper explores a much simpler strategy of passive flow control that may have the potential for application to at least somewhat wider flow conditions. The idea is to use impinging devices in

the form of finite circular cylinders with the aim to produce counter-rotating wake vortices and longitudinal streaks capable of delaying and suppressing flow separation. Despite similarities with more common vortex generators, the control effect of impinging devices has its origin in a different flow control mechanism and is less dependent on the flow direction of the surrounding flow because of the axisymmetric shape of the actuator. Note however that even impinging devices are dependent on the thickness of the boundary layer and thus are optimized for a particular Reynolds number. The important advantage of the impinging device over other flow control strategies is its extreme simplicity, which could make it a partial solution for drag reduction in the near future.

## AHMED BODY WITH IMPINGING DEVICES

The passive flow control case studied in the present work is that of the generic car model called the Ahmed body, which has previously been studied in both experimental (e.g. Ahmed [1], Lienhart et al. [2]) and numerical work (Krajnović and Davidson [3, 4] and Basara et al. [5]). The geometry of the body is given in Fig. 1.

All the geometric quantities are normalized with the body height, $H$, which is equal to 0.288 m. The values of the geometric quantities are $L/H = 3.625$ and $l/H = 0.697$ and the width $W/H = 1.35$. The front part is rounded with a radius of $0.347H$ in the planes, $y = 0$ and $z = 0$. The geometry of the rounded corners was made from the data (in the form of distinct points) measured at the body used in Ahmed *et al.* [1] and Lienhart and Becker [2]. The angle of the rear slanted surface is $25^o$ and the free-stream velocity is 20 m/s, resulting in a Reynolds number based on the model length $L$ of $Re_L = 1.35 \times 10^6$. This body is placed in the channel with a cross section of $6.493H \times 4.861H$ (width $\times$ height). The cross section of this channel is identical to the open test section of the wind tunnel used in the experiments of Lienhart and Becker [2]. The front face of the body is located at a distance of $7.3H$ from the channel inlet and the downstream length between the rear face of the body, and the channel outlet is $21H$. The body is lifted from the floor, producing a ground clearance of $0.174H$, as in the experiments.

In a previous experimental study, Pujals et al. [6] used the cylindrical roughness elements presented in Fig. 2 to force the large-scale streaks. They studied several cylinder configurations, changing the height of the cylinders, $k$, their diameter, $d$, the spanwise spacing, $\lambda_z$, and the distance from the roughness to the rear slanted surface of the body, $x_o$. The experimental study by Pujals et al. [6] showed that the configuration of the roughness with 16 cylinders and $\lambda_z = 24$mm, $d = 6$mm, $k = 12$mm and $x_o = 120$mm resulted in a maximum drag reduction of approximately 10%. That configuration of the cylindrical roughness was chosen in the present study. The same flow was computed in [7] using Partially-Averaged Navier-Stokes (PANS) simulation. However, PANS was found inadequate for prediction of this flow.

## FLOW CONTROL MECHANISM

One way to delay or suppress the separation at the rear end of a vehicle is to add momentum in the near-wall region of the boundary layer. Enriching the energy content of the near-wall region will help to prevent the separation due to the adverse pressure gradient. This effect can be achieved with passive flow devices such as vortex generators (VGs). The idea of using vortex generators is borrowed from aeronautical engineering, and counter-rotating VGs producing two counter-rotating vortices are found to be more efficient than co-rotating VGs. These VGs interact with the main flow and produce strong counter-rotating vortices. These vortices push high momentum fluid from the upper boundary layer region into the low energetic near-wall region. One disadvantage of VGs is that their efficiency is dependent on the angle of attack of the incoming flow. Ground vehicles are often influenced by crosswinds leading to variations in the angle of the incoming flow. Another approach for passive flow control is to use so called impinging devices in the form of small bluff bodies placed upstream of the expected location of the flow separation. These devices should not be called VGs as their influence on the downstream boundary layer and the resulting wake flow is different from that of VGs. The present work uses such impinging devices in the form of short finite cylinders (Figs. 2 and 3). These devices are here denoted impinging devices as the impinging of the flow on the bluff bodies underplays the flow mechanism resulting in the formation of downstream streaks. These streaks are different from the streamwise vortices downstream of the VGs. The flow mechanism is that high momentum fluid is pushed toward the low energy near-wall flow but at the same time low momentum fluid is pushed away from the wall, resulting in streamwise elongated streaks. These streaks are much weaker than the vortices generated by VGs, and we will demonstrate their formation and the influence on the generic vehicle flow studied here.

## NUMERICAL DETAILS

The governing LES equations are the incompressible Navier-Stokes and the continuity equations filtered with the implicit spatial filter of characteristic width $\Delta$. The filter width, $\Delta$, is defined in this work as $\Delta = (\Delta_1\Delta_2\Delta_3)^{1/3}$, where $\Delta_i$ are the computational cell sizes in three coordinate directions. The algebraic eddy viscosity model originally proposed by [8] is used in this paper. The value of Smagorinsky constant $C_s = 0.1$ previously used for bluff-body flows [9, 10], flow around a

simplified bus [11], generic trains [12, 13] and generic car called Ahmed body [3] is used in this work. Using the Van Driest damping function $f = 1 - \exp(-n^+/25)$ (here, $n^+ = nu_\tau/\nu$), wall effects are partially taken into account by 'damping' length scale $l = C_s\Delta$ near the walls.

A uniform velocity profile, $U_\infty = 20$ m/s, constant in time was used as the inlet boundary condition. The homogeneous Neumann boundary condition was used at the downstream boundary. The lateral surfaces and the ceiling were treated as slip surfaces. No-slip boundary conditions were used on the surface of the body and the channel floor.

LES equations are discretized with a commercial finite volume solver, AVL FIRE, to solve the incompressible Navier-Stokes equations using a collocated grid arrangement. Convective fluxes are approximated by a blend of 98% central differences of second-order accuracy and of 2% upwind differences. The time integration is done using the second-order accurate, three-time level Euler scheme. The same numerical discretization has previously been used for LES of several bluff-body flows ([14],[15],[16],[17]).

Computational grids were made using ICEM-CFD grid generator. Accuracy was established by making simulations on several different multi-block hexahedral conforming computational grids.

The computational grids were different for the natural and the controlled flows. For the natural flow, a computational grid of approximately 16 million computational cells was used. Three different computational grids were used for the flow with cylindrical roughness, containing approximately 18, 30 and 50 million cells. The wall normal resolution of all computational grids was below $y^+ = 1$. The resolution in the streamwise direction varied between 50 and 250 wall units. The spanwise resolution was between approximately 20 and 80 wall units, with a wide spread for the controlled flow due to the presence of the cylinders. The authors previous work [18] showed that the LES of the flow around a finite circular cylinder requires very fine computational grids and, with 16 cylinders in the present configuration, the well resolved LES of this flow will require much more than the 50 million cells used in the present simulation. Although it is assumed that it will be difficult to achieve an adequate LES resolution to completely resolve the cylinder flows, it is expected that the prediction of the origin and development of the counter-rotating streamwise vortices in the cylinders wakes can be achieved with a somewhat coarser grid. The resolution requirements for prediction of the flow control structures are not known at the present stage, and one of the aims of this work is to find these requirements from comparisons of the LES results with the experimental data.

## INFLUENCE OF THE CYLINDERS ON THE DOWNSTREAM FLOW

Figure 3 shows the time-averaged flow around some of the cylinders. The time-averaged cylinder flow consists of several flow features, such as a horse-shoe vortex and separation bubbles on the free end and in the near wake. However, for the purpose of the present investigation, the formation of the counter-rotating vortices directly after the near-wake bubble is the important flow mechanism. These vortices are the indirect cause of the flow control, and they will be discussed in the following text. More about the complete representation of the flow around finite cylinder can be found in [18]. Figures 4 - 6 show the instantaneous flow structures behind the cylinders. The identification of the counter-rotating vortices in the instantaneous flow is not simple, and most of the analyses in the present work will use the time-averaged flow, which shows the mean effect of the flow control. An important message to be derived from Figs. 4 and 5 is that several coherent structures behind cylinders interact, resulting in the mean counter-rotating vortices. The mean counter-rotating vortices seen in Fig. 7 are not present at any downstream location or time in the instantaneous flow.

Figures 7 and 8 illustrate the downstream development of the time-averaged flow structures behind the cylinders. Two effects on the cylinders downstream flow can be seen in these figures. The incoming flow interacting with the cylinders results in the formation of the streamwise vortices indicated in Fig. 7 with the magnitude of the streamwise vorticity component $\omega_x$. These vortices are not very strong, however, and they quickly lose strength. As seen in Fig. 7, they have almost disappeared at the position of the flow separation at the leading sharp edge of the slanted surface (Fig.7k). Another effect of the cylinder on the downstream flow is the spanwise modulations of the streamwise velocity component shown in Figs. 6 and 8. At the same time as the strength of the streamwise vortices in Fig. 7 decreases and becomes rather weak at $x/\lambda_z = -0.9$, the modulation of $\overline{u}/U_e$ in the spanwise direction becomes very strong. At the position of the flow separation, where the streamvise vorticies have virtually vanished (Fig. 7k), the spanvise modulations of the streamvise velocity are still present (Figs. 6k and 8k). In the case of counter-roating VGs, we would expect to see much stronger streamwise vortices than those seen in Figs. 5 and 7. However, in the case of cylinders, as used in the present work, it is not the effect of the stramwise vortices that affects the separation downstream but the modulation of the streamvise velocity seen in Figs. 6 and 8. Figure 6 shows the existence of high-speed streaks (warmer colors) and low-speed streaks (cold colors). Note the very strong low-speed streaks even at the position of the sharp edge of the slanted surface (Fig. 6k). The question is how these steaks alone can lead to suppression of the separation region if the streamwise vortices are too weak to influence the separation at the sharp edge of the slanted surface and downstream. The counter-rotating vortices shown in Fig. 7 modify the boundary layer downstream of the cylinders. They act as redistributors of the velocity in the boundary layer, bringing down the high velocity from the upper parts of the boundary layer to the near-wall region and lifting up the lower velocity fluid from the near-wall region to the upper part of the boundary layer. As seen in Fig. 7, the position of the counter-rotating streamwise vortices in pairs behind each cylinder leads to an accelerated streamwise velocity $\overline{u}/U_e$ in the wakes of the cylinders, while the low

$\overline{u}/U_e$ occurs at spanwise positions between the cylinders.

The resolved Reynolds stresses are shown downstream of the cylinders in Figs. 9- 11. The distribution of high levels of the normal Reynolds stresses (and thus the turbulent kinetic energy) in the near wake of the cylinders and lower levels in the regions downstream of the gaps between the cylinders already changes at the position $x/\lambda_z = -3.0$ (Figs. 9d) for the stress in the streamwise direction $\overline{u}^2$. The stresses in the other two directions experience a similar behavior further downstream. This leads to low levels of turbulent kinetic energy in the far wakes of cylinders and increased kinetic energy between the spanwise positions of the cylinders at the location of the sharp edge separation. Beside the observation of the redistribution of the turbulent kinetic energy between the near wake and far wake regions behind cylinders, the total turbulent kinetic energy in the boundary layer at the position of separation is found to be increased as compared to natural flow. It is this increase in turbulent kinetic energy in the boundary layer, leading to increased momentum transfer in combination with the increased streamwise velocity in the near-wall regions, that influences the flow downstream of the sharp leading edge of the slanted surface.

Note that the levels of high normal Reynolds stresses (leading to high turbulent kinetic energy) coincide with the location of low-speed streaks. The streaks extend downstream of the separation line, and that is visualized in Fig. 12. One can observe the modulation of the streamvise velocity in the spanwise direction seen in Fig. 12 as the waviness of the isosurface of $\overline{u}/U_e$ long downstream of the separation. This leads to suppression of the separation region on the slanted surface of the body.

One interesting observation in Figs. 7-8 is that the spanwise distribution of the streamwise vortices and streaks is not uniform. The reason for this is found in the three-dimensionality of the flow. Both the streamwise vortices and the streaks are found to be stronger away from the symmetry plane of the body.

The distribution of the streamwise velocity component $\overline{u}/U_e$ at height $y/k = 0.5$ ($y = 6$mm) in Fig. 13a shows regions of low-speed (cold colors) and high-speed streaks (warm colors). There are different ways to study the growth of the streaks in the streamwise direction. For example, the energy amplification used in linear stability analyses or the min-max criterion expressing the difference between the velocitities in the high and the low speed streaks ([19]) can be used. The amplitude of the streaks in the present work is measured using the definition of a local min-max criterion in [6]

$$\hat{A}_{st}(x,y/k) = \frac{\overline{u}(x,y/k,z_{hsst}) - \overline{u}(x,y/k,z_{lsst})}{2U_e} \tag{1}$$

where $z_{hsst}$ denotes the spanwise location of high-speed streaks ($z/\lambda_z = \pm 0.5, \pm 1.5, \pm 2.5, ...$) and $z_{lsst}$ denotes the location of the low-speed streaks ($z/\lambda_z = 0, \pm 1, \pm 2, ...$). This definition was used in the present work in order to simplify comparison with the experimental observations from [6]. Figure 13 shows $\hat{A}_{st}(x,y/k = 0.5)$ for different spanwise positions of the body. The strength of the streaks decreases away from the symmetry plane of the body. The algebraic growth of the streaks observed in the experiments [6] is found at all spanwise positions with a maximum in the symmetry plane with an amplitude of between $6-7\%$ of $U_e$. The amplitude of the streaks averaged in the spanwise direction is shown with a solid line in Fig. 13. The maximum averaged amplitude is reached at approximately $x/\lambda_z = 2.4$, in agreement with the experimental observation. The maximum amplitude of the averaged value is 5% of $U_e$ which is lower than 9% of $U_e$ found in the experiment.

**TIME-AVERAGED FLOW**

Figure 14 shows the resulting time-averaged flow structures in the near wake of the body and around the slanted surface. The influence of the streaks on the time-averaged flow is found to be rather strong. The recirculation region on the slanted surface is considerable reduced in both length and thickness (Figs. 15 and 16). The indirect influence of this damping of the separation bubble on the slanted surface is that the trailing vortices gain in strength. Figure 14 shows longer vortex cores of the trailing vortices in the controlled flow, indicating stronger vortices. This difference in the trailing vortices has direct influence on the near wake flow. Two horse-shoe vortices placed one above the other are visible in the near wake of the natural flow. The legs of these vortices seem to be weakened and anihilated by the influence of stronger trailing vortices in the controlled flow (Fig. 14b).

Figure 17 shows the development of the streamwise vorticity component $\omega_x$ behind the body. In agreement with the observations of the vortex cores in Fig. 14, this figure shows the more concentrated vorticity in the trailing vortices of the controlled case. The explanation for the stronger trailing vortices in the controlled case is found in a reduction of the transversal separation bubble on the slanted surface that leaves more space for trailing vortices. These vortices are drag inducing and, although they contribute to the total drag, the smaller destruction of the turbulent kinetic energy on the slanted surface due to a smaller separation region in controlled flow leads to a larger savings, which give a reduction in net drag.

Although the length of the separation bubble on the slanted surface is drastically decreased in Fig. 15, the trace lines in Fig. 15b show the existence of the transversal separation bubble in the LES results. The experimental data in [6] showed completely attached flow in this region. The side view of the streamlines projected on the symmetry plane (Fig. 16) shows that the separation bubble in the LES using the finest grid is extremely thin. The velocity field in the experiments was

measured at a distance of $y/k = 0.08$, and it is possible that a separation bubble exists in the experimental flow but that it is located below this plane. However, the same position of the velocity plane from LES shows a weak separation bubble, leading to the conclusion of there being differences in the experimental and LES flows. The probable explanation is that there is still a potential in grid refinement which would lead to even better agreement with the experimental data. Figure 16 shows that the refinement of the computational grid from medium to fine leads to strong damping of the separation bubble on the slanted surface of the body. The drag reduction effect is a combined result of several contributors. The most obvious is the pressure increase on the slanted surface due to the absence of a transversal separation bubble on the slanted surface. Figure 16 shows an elongation of the near wake separation bubble, which may also have effects on the surface pressure on the vertical base of the body.

## COMPARISSON WITH EXPERIMENTAL DATA

Figures 18 and 19 show the velocity and pressure, respectively, near the slanted surface from the LES results. The natural flow predicted in the LES is in good agreement with the experimental data [6]. The prediction of the controlled flow in Fig. 18b shows a nearly attached flow but, as discussed earlier, a weak separation near the leading edge of the slanted surface is visible in the LES but not in the experiments [6]. As a consequence of such a difference in the velocity field between the LES and the experiments, a slightly lower pressure in the upper region of the slanted surface is visible in Fig. 19b compared with that in the experiment [6]. A comparison of the surface pressure coefficient $C_p$ in the symmetry plane of the slanted surface and the vertical base of the body between different simulations and the experimental data is shown in Fig. 20. Experimental data are available only at the slanted surface. The agreement of the predicted $C_p$ in the natural flow with the experimental data is good everywhere except between $x = 0$ and $x = 0.02$m. The agreement of the LES predicted controlled flow is poorer than for the natural flow. The trends in the LES are found to be in good agreement, and the grid refinement leads to better results, but the $C_p$ curve is somewhat shifted and the surface pressure coefficient directly after the leading edge of the slanted surface is far too low. The conclusion is that a refined computational grid is required for a LES solution that converges to the experimental data. The pressure distribution on the vertical base of the body showed only small differences between the natural flow and the controlled flow LES using the fine grid. Note that an insufficient resolution (medium grid) leads to a false conclusion of an increased $C_p$ at the base.

## GRID REFINEMENT

The computational grid used for the natural flow is identical to that used in the previous LES [3] of the flow around this body but at Reynolds number of $2 \times 10^5$ based on the inlet velocity and the height of the body. The higher Reynolds number of the flow in the present paper requires much finer computational grid. However, because of limited computational resources it was necessary to make a choice if the grid refinement should be made for the natural or the controlled flow and it was decided to concentrate the study on the controlled flow. The consequence of the unresolved natural flow LES is that the predicted drag coefficient was $C_d^o = 0.325$ which is 9% higher than the experimental value of $C_d^{oEXP} = 0.298$ from [1]. Note, however, that the Reynolds number of the experimental flow was $1.2 \times 10^6$ which is four times higher from the Reynolds number used in this paper. Although there is some influence of the Reynolds number on the drag coefficient, it is expected not to be large between $Re = 3 \times 10^5$ and $Re = 1.2 \times 10^6$. Unfortunately, no absolute values of the drag coefficient were presented in [6] at $Re = 3 \times 10^5$. It was therefore decided to use the experimental value from [1] and the LES value on unresolved grid from the present work as references for the natural flow drag coefficient. The drag reduction that results from the passive flow control applied to the Ahmed body is quantified in the present work by $\Delta C_d$, defined as $\Delta C_d = 2(C_d - C_d^o)/(C_d + C_d^o)$, where $C_d^o$ and $C_d$ are the time-averaged drag coefficients of the natural and controlled flow, respectively. The same quantity was computed in the experimental work by Pujals et al. [6]. $\Delta C_d^{LES}$ was found to be 24%, 22% and 11.6% for the coarse, medium and fine grid LES when we use $C_d^{oEXP} = 0.298$ from the experiment by [1]. If we on the other hand use $C_d^o = 0.325$ for the natural flow computed in the present work, the drag reduction is 13.9%, 11.7% and 3%. The value obtained in the experiments by Pujals et al. [6] was around $\Delta C_d^{EXP} = 10\%$, which is close to the present LES prediction using fine grid if $C_d^{oEXP} = 0.298$ is used as a reference for the natural flow. The results of the mesh refinement study don't show proof for mesh converged LES and there is still room for mesh refinement. However, the fine grid LES produced the flow in sufficiently good agreement with the experimental observations that it could be used to study of the flow control mechanism used on the body. To increase our knowledge of the flow control mechanism using impinging devices was the main aim of the present paper and the results of the present LES were found to be a useful tool for the exploration of the flow. Furthermore, the grid refinement study has shown the possibilities and limitations of such LES.

## CONCLUSIONS

The application of the impinging devices for passive flow control with the aim of reducing the drag of a simplified vehicle is explored using LES. The aim of the study was to explore the capability of LES to predict such passive flow

control. The previous experience of high resolution requirements of the LES for a combination of bluff bodies (i.e. the vehicle and the cylinders) is found to be an obstacle to obtaining exact agreement with experimental observations. However, the flow control effect was successfully predicted with relatively moderate resolution for the Reynolds number used in the study. The mesh refinement study indicates a substantial improvement of the results with a relatively small increase in the number of computational cells, and this, together with the comparison with the experimental data, gives hope that the present resolution is close to the sufficient LES resolution of this flow. The second objective of the study was to increase our knowledge of the flow control mechanism using impinging devices. The two-stage flow control process starts with the formation of the counter-rotating streamwise vortices just behind the near wake of the cylindrical impinging devices. These vortices are responsible for the formation of the energetic streaks further downstream. These streaks influence the flow all the way downstream of the separation line. The low-speed streaks are particularly found to contain high turbulent kinetic energy that influences the shear layer and the mixing in the transversal separation bubble on the slanted surface. This results in a strong damping of the separation region on the slanted surface and an increase in the strength of the vortices trailing around the slanted lateral edges of the rear. The change in size of these two flow structures leads to a modification of the near wake and a longer separation bubble behind the vertical base. The net effect of the actuation is a decrease in the aerodynamics drag. The drag reduction in the present LES is somewhat lower than that found in the experiments, probably as a result of the insufficient grid resolution. The flow control approach used in the present study shows good potential. No moving parts or active flow control are used, and the shape of the impinging bodies (cylindrical) makes the flow control efficient even if the incoming flow is yawed (at least at small yaw angles).

**Achnowledgements**

The work presented here was funded by Trafikverket and the Chalmers Sustainable Transport Initiative. The author is grateful to Dr. Pujals from PSA for providing his experimental data for comparison with authors LES results. AVL List GmbH provided the licenses for the AVL FIRE solver for the project. Computations were performed at Swedish National Infrastructure for Computing (SNIC) at the Center for Scientific Computing at Chalmers (C3SE).

**References**

[1] S. R. Ahmed, G. Ramm, and G. Faltin. Some salient features of the time averaged ground vehicle wake. SAE Paper 840300, 1984.

[2] H. Lienhart and S. Becker. Flow and turbulent structure in the wake of a simplified car model. SAE Paper 2003-01-0656, 2003.

[3] S. Krajnović and L. Davidson. Flow around a simplified car, part 1: Large eddy simulation. *ASME: Journal of Fluids Engineering*, 127:907–918, 2005.

[4] S. Krajnović and L. Davidson. Flow around a simplified car, part 2: Understanding the flow. *ASME: Journal of Fluids Engineering*, 127:919–928, 2005.

[5] B. Basara, S. Krajnović, and S. Girimaji. Pans vs. les for computing of the flow around a 3d bluff body. In *7th International ERCOFTAC Symposium on Engineering Turbulence Modelling and Measurements*, Limassol, Cyprus, 4-6 June, 2008.

[6] G. Pujals, S. Depardon, and C. Cossu. Drag reduction of a 3d bluff body using coherent streamwise streaks. *Experiments in Fluids*, 49:1085–1094, 2010.

[7] S. Krajnović and X. Han. Les and pans of passive and active control of flows around generic vehicle bodies. In *Seventh International Conference on Computational Fluid Dynamics (ICCFD7)*, Big Island, Hawaii, 2012.

[8] J. Smagorinsky. General circulation experiments with the primitive equations. *Monthly Weather Review*, 91(3):99–165, 1963.

[9] S. Krajnović and L. Davidson. Large eddy simulation of the flow around a bluff body. *AIAA Journal*, 40(5):927–936, 2002.

[10] S. Krajnović. LES of flows around ground vehicles and other bluff bodies. *Philosophical Transactions of The Royal Society A*, 367 (1899):2917–2930, 2009.

[11] S. Krajnović and L. Davidson. Numerical study of the flow around the bus-shaped body. *ASME: Journal of Fluids Engineering*, 125:500–509, 2003.

[12] H. Hemida and S. Krajnović. LES study of the influence of train nose shape on the flow structures under cross-wind conditions. *ASME: Journal of Fluids Engineering*, 130, 2008.

[13] S. Krajnović, P. Ringqvist, K. Nakade, and B. Basara. Large eddy simulation of the flow around a simplified train moving through a crosswind flow. *Journal of Wind Engineering and Industrial Aerodynamics*, 110:86–99, 2012.

[14] S. Krajnović, A. Bengtsson, and B. Basara. Large eddy simulation investigation of the hysteresis effects in the flow around an oscillating ground vehicle. *ASME: Journal of Fluids Engineering*, 133:121103, 2011.

[15] S. Krajnović, S. Sarmast, and B. Basara. Numerical investigation of the flow around a simplified wheel in a wheelhouse. *ASME: Journal of Fluids Engineering*, 133:111001, 2011.

[16] S. Krajnović, J. Östh, and B. Basara. LES study of breakdown control of a-pillar vortex. *International Journal of Flow Control*, 2(4):237–257, 2011.

[17] J. Östh and S. Krajnović. The flow around a simplified tractor−trailer model studied by large eddy simulation. *Journal of Wind Engineering and Industrial Aerodynamics*, 102:36–47, 2012.

[18] S. Krajnović. Flow around a tall finite cylinder explored by large eddy simulation. *Journal of Fluid Mechanics*, 676:294–317, 2011.

[19] P. Andersson, L. Brandt, A. Bottaro, and D. Henningson. On the breakdown of boundary layers streaks. *Journal of Fluid Mechanics*, 428:29–60, 2001.

**List of Figures**

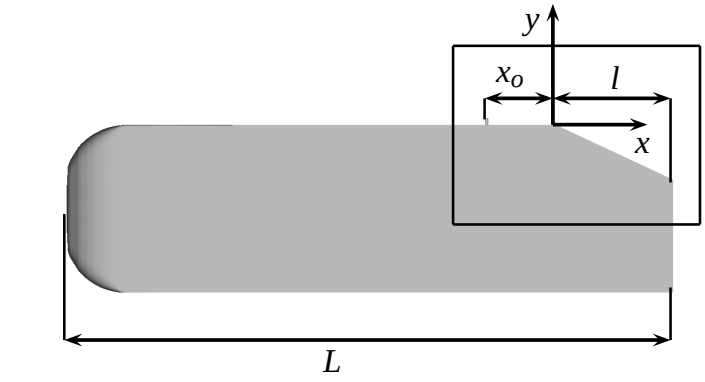


a)

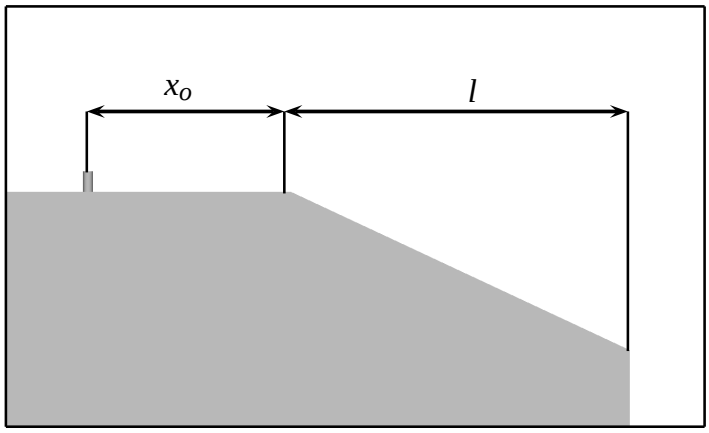


b)

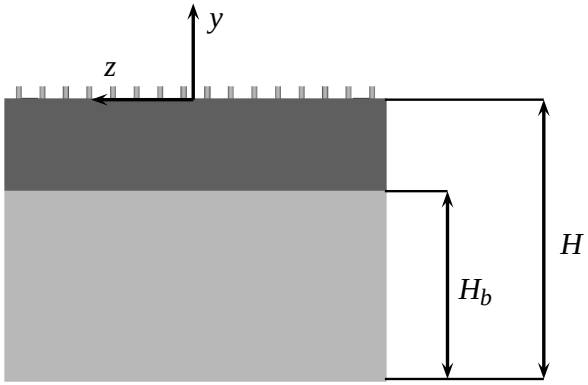


c)

Fig. 1: a) Shape of the Ahmed body. b) Zoom of the rear of the geometry. c) Ahmed body seen from behind.

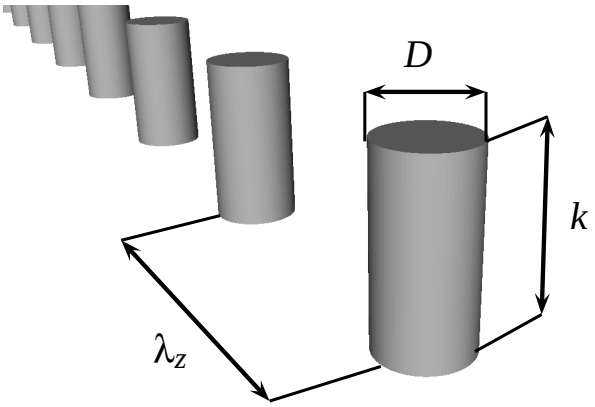


Fig. 2: The relevant parameters of the cylindrical roughness elements.

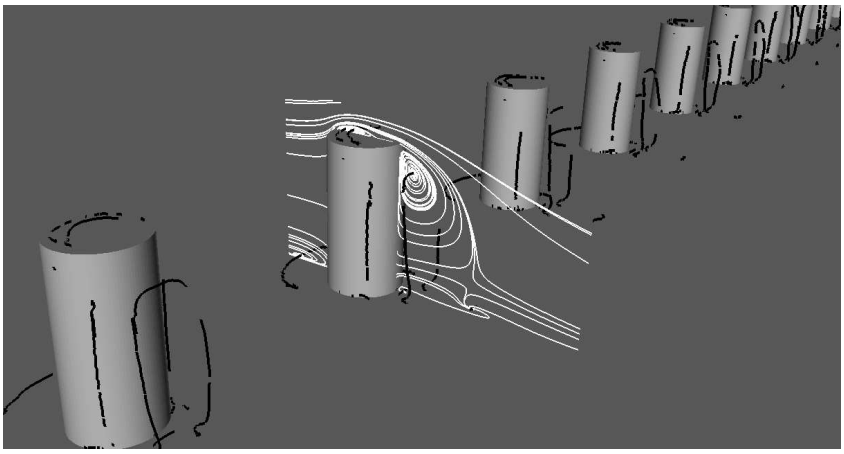

Fig. 3: Time-averaged flow around the cylinders. Vortex cores are shown in black and streamlines projected onto the symmetry plane are shown in white. Flow is from left to right.

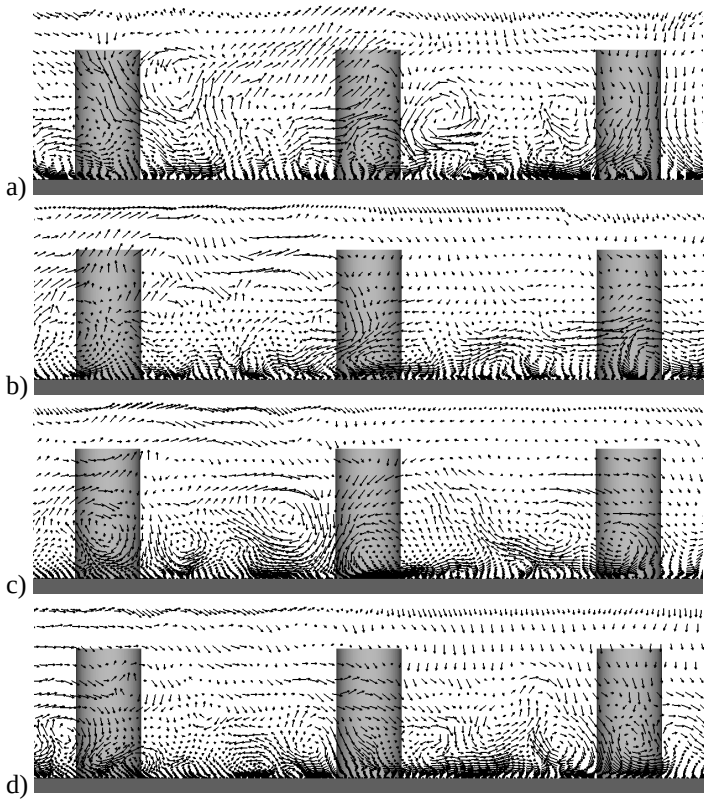


Fig. 4: Planes of the instantaneous velocity at a) $x/\lambda_z = -2.5$, b) $x/\lambda_z = -1.7$, c) $x/\lambda_z = -0.9$, d) $x/\lambda_z = -0.05$.

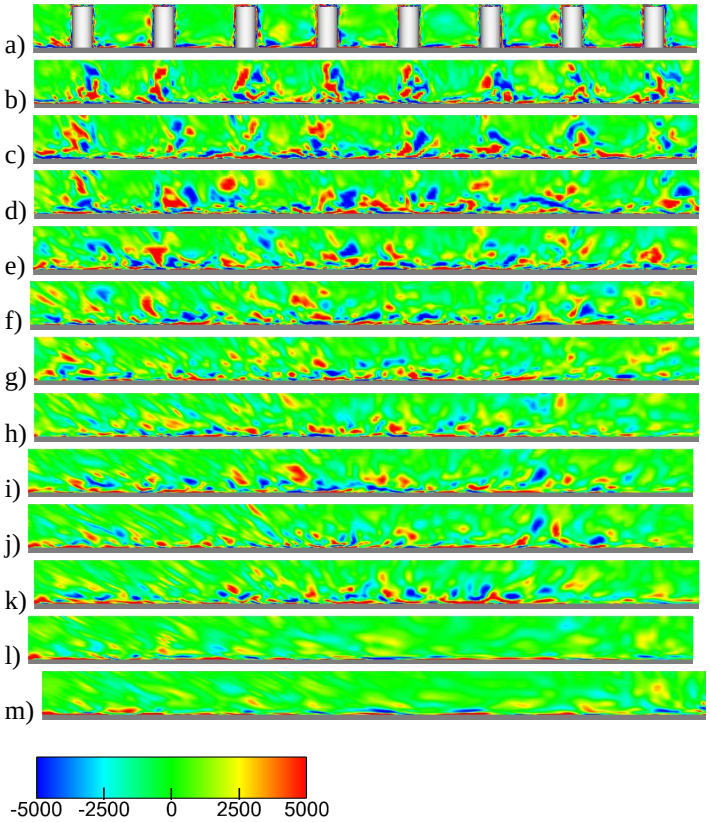


Fig. 5: Planes of the instantaneous streamwise vorticity, $\omega_x$, at: a) $x/\lambda_z = -4.2$, b) $x/\lambda_z = -3.8$, c) $x/\lambda_z = -3.4$, d) $x/\lambda_z = -3.0$, e) $x/\lambda_z = -2.5$, f) $x/\lambda_z = -2.1$, g) $x/\lambda_z = -1.7$, h) $x/\lambda_z = -1.3$, i) $x/\lambda_z = -0.9$, j) $x/\lambda_z = -0.5$, k) $x/\lambda_z = -0.05$, l) $x/\lambda_z = 0.4$ and m) $x/\lambda_z = 0.8$.

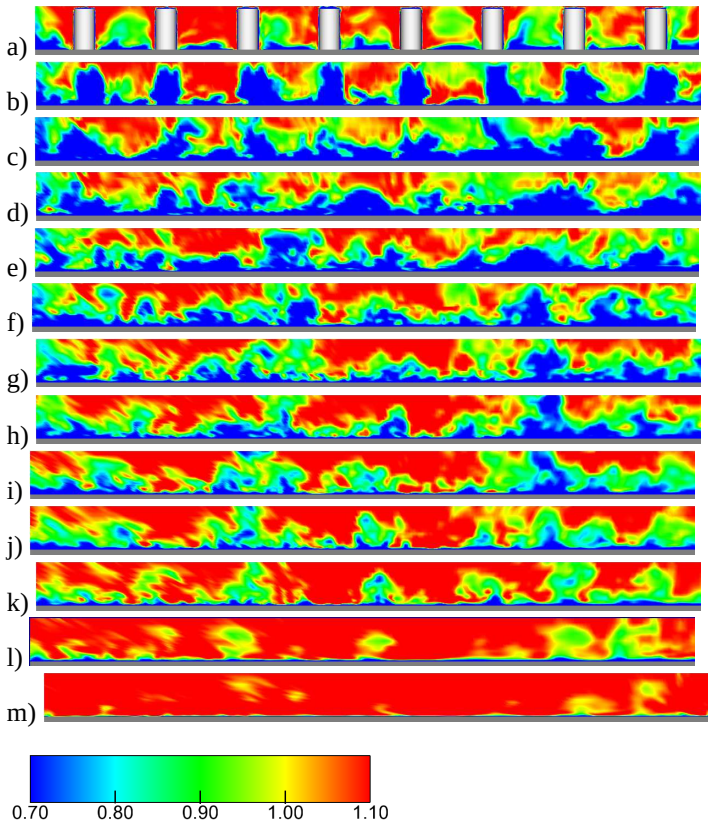


Fig. 6: Planes of the instantaneous streamwise velocity, $\overline{u}/U_e$, at: a) $x/\lambda_z = -4.2$, b) $x/\lambda_z = -3.8$, c) $x/\lambda_z = -3.4$, d) $x/\lambda_z = -3.0$, e) $x/\lambda_z = -2.5$, f) $x/\lambda_z = -2.1$, g) $x/\lambda_z = -1.7$, h) $x/\lambda_z = -1.3$, i) $x/\lambda_z = -0.9$, j) $x/\lambda_z = -0.5$, k) $x/\lambda_z = -0.05$, l) $x/\lambda_z = 0.4$ and m) $x/\lambda_z = 0.8$.

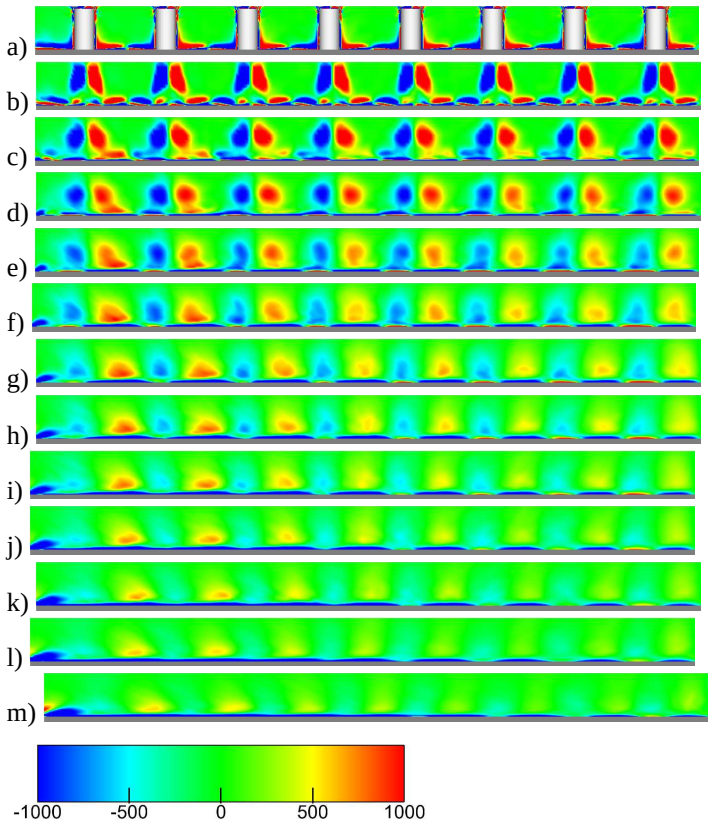


Fig. 7: Planes of the time-averaged streamwise vorticity, $\omega_x$, at: a) $x/\lambda_z = -4.2$, b) $x/\lambda_z = -3.8$, c) $x/\lambda_z = -3.4$, d) $x/\lambda_z = -3.0$, e) $x/\lambda_z = -2.5$, f) $x/\lambda_z = -2.1$, g) $x/\lambda_z = -1.7$, h) $x/\lambda_z = -1.3$, i) $x/\lambda_z = -0.9$, j) $x/\lambda_z = -0.5$, k) $x/\lambda_z = -0.05$, l) $x/\lambda_z = 0.4$ and m) $x/\lambda_z = 0.8$.

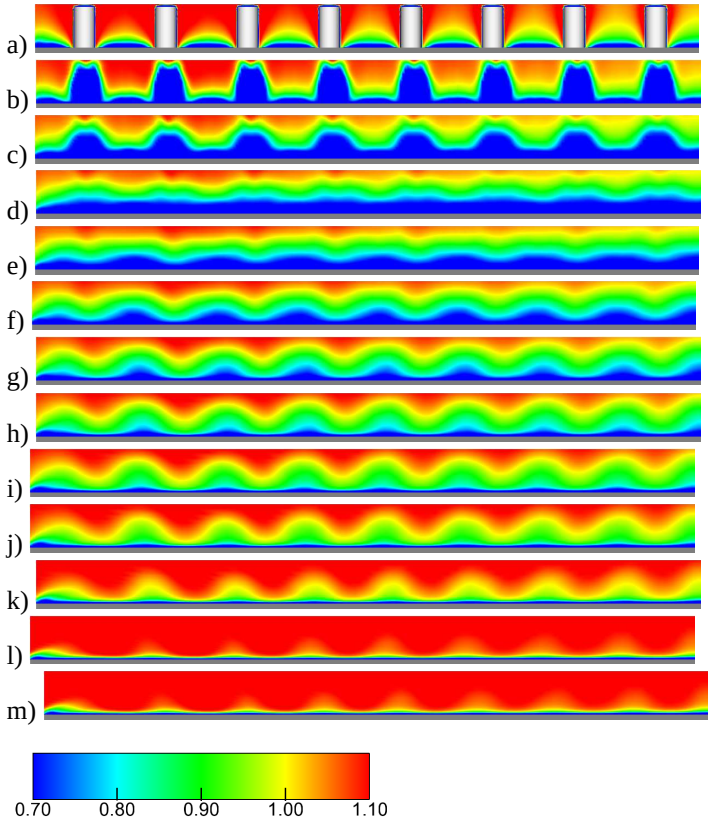


Fig. 8: Planes of the time-averaged streamwise velocity, $\overline{u}/U_e$, at: a) $x/\lambda_z = -4.2$, b) $x/\lambda_z = -3.8$, c) $x/\lambda_z = -3.4$, d) $x/\lambda_z = -3.0$, e) $x/\lambda_z = -2.5$, f) $x/\lambda_z = -2.1$, g) $x/\lambda_z = -1.7$, h) $x/\lambda_z = -1.3$, i) $x/\lambda_z = -0.9$, j) $x/\lambda_z = -0.5$, k) $x/\lambda_z = -0.05$, l) $x/\lambda_z = 0.4$ and m) $x/\lambda_z = 0.8$.

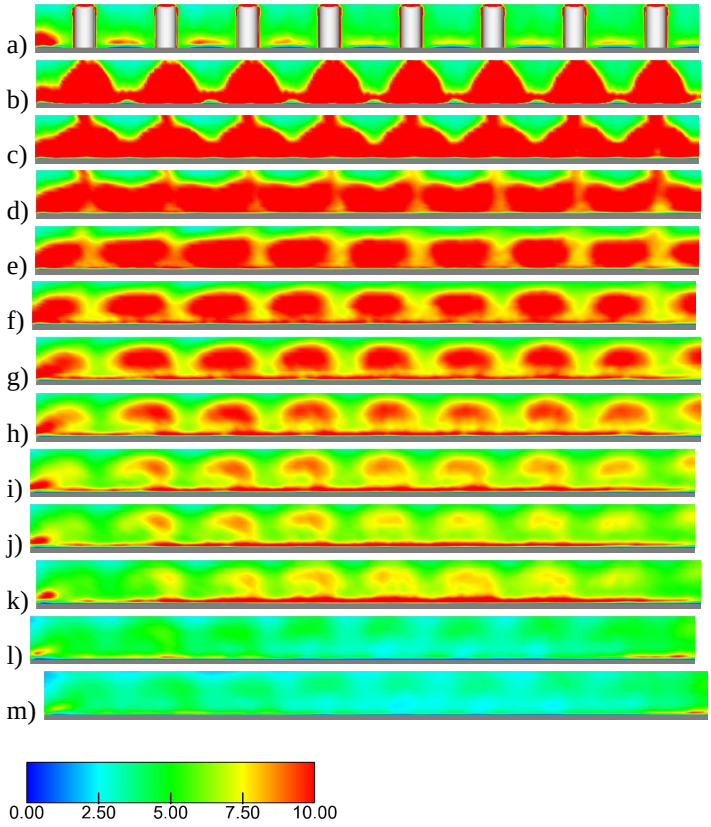


Fig. 9: Planes of the resolved Reynolds stress in $m^2/s^2$ in the streamwise direction, $\overline{u}^2$, at: a) $x/\lambda_z = -4.2$, b) $x/\lambda_z = -3.8$, c) $x/\lambda_z = -3.4$, d) $x/\lambda_z = -3.0$, e) $x/\lambda_z = -2.5$, f) $x/\lambda_z = -2.1$, g) $x/\lambda_z = -1.7$, h) $x/\lambda_z = -1.3$, i) $x/\lambda_z = -0.9$, j) $x/\lambda_z = -0.5$, k) $x/\lambda_z = -0.05$, l) $x/\lambda_z = 0.4$ and m) $x/\lambda_z = 0.8$.

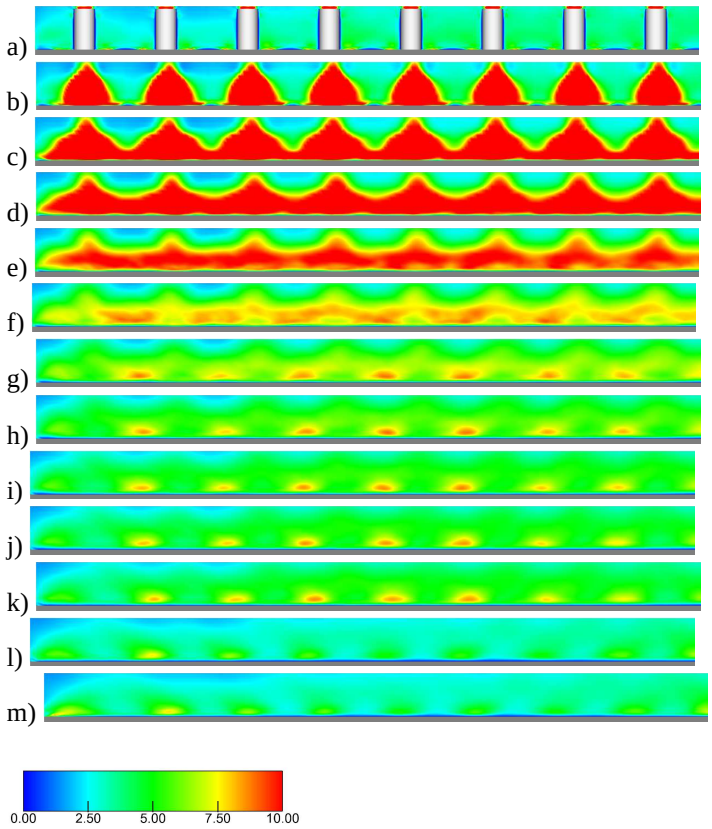


Fig. 10: Planes of the resolved Reynolds stress in $m^2/s^2$ in the spanwise direction, $\overline{w}^2$, at: a) $x/\lambda_z = -4.2$, b) $x/\lambda_z = -3.8$, c) $x/\lambda_z = -3.4$, d) $x/\lambda_z = -3.0$, e) $x/\lambda_z = -2.5$, f) $x/\lambda_z = -2.1$, g) $x/\lambda_z = -1.7$, h) $x/\lambda_z = -1.3$, i) $x/\lambda_z = -0.9$, j) $x/\lambda_z = -0.5$, k) $x/\lambda_z = -0.05$, l) $x/\lambda_z = 0.4$ and m) $x/\lambda_z = 0.8$.

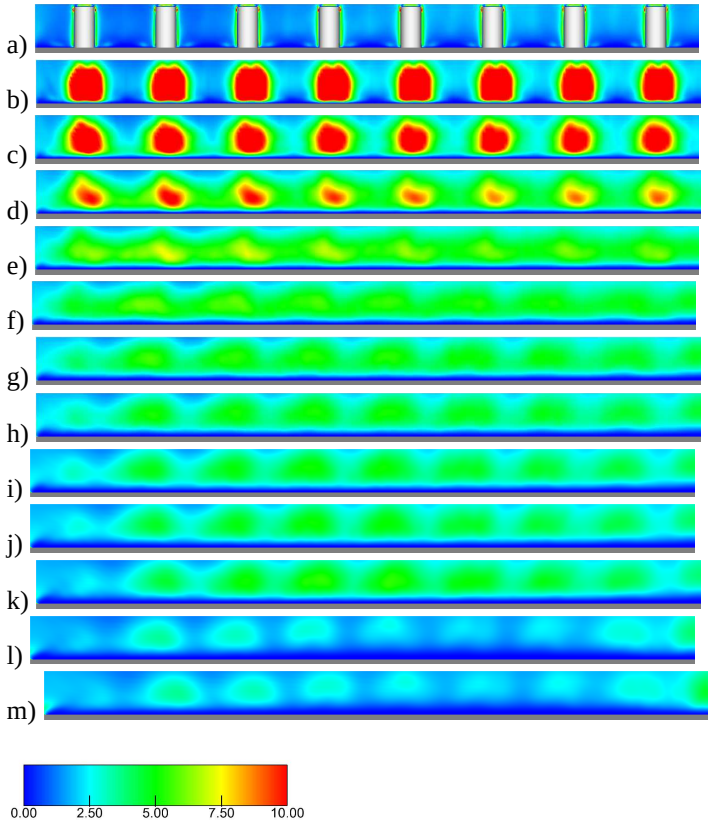


Fig. 11: Planes of the resolved Reynolds stress in $m^2/s^2$ in the wall normal direction, $\overline{v'^2}$, at: a) $x/\lambda_z = -4.2$, b) $x/\lambda_z = -3.8$, c) $x/\lambda_z = -3.4$, d) $x/\lambda_z = -3.0$, e) $x/\lambda_z = -2.5$, f) $x/\lambda_z = -2.1$, g) $x/\lambda_z = -1.7$, h) $x/\lambda_z = -1.3$, i) $x/\lambda_z = -0.9$, j) $x/\lambda_z = -0.5$, k) $x/\lambda_z = -0.05$, l) $x/\lambda_z = 0.4$ and m) $x/\lambda_z = 0.8$.

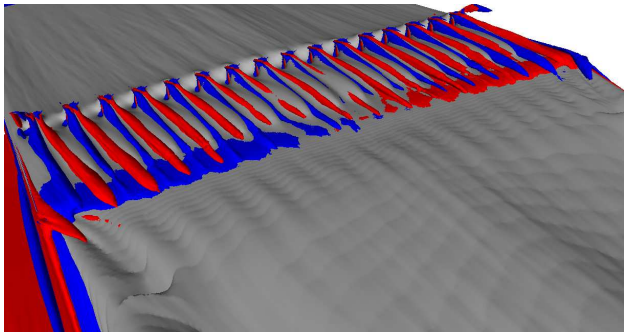

Fig. 12: Counter-rotating vortices visualized using isosurfaces of the time-averaged streamwise vorticity component $\omega_x = \pm 300$. The streaks are shown using an isosurface of $\overline{u}/U_e = 0.95$.

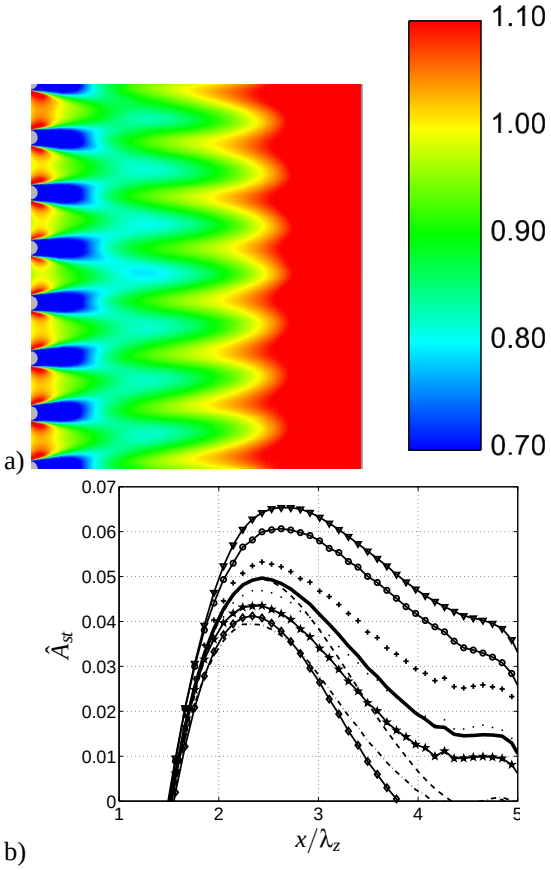


Fig. 13: a) Velocity streaks on the roof of the model at $y/k = 0.5$ from the wall. The flow is from left to right. b) The amplitude of the streaks $\hat{A}_{st}(x, y/k = 0.5)$ as a function of the the distance from the cylinders array scaled with the spanwise spacing $\tilde{x}/\lambda_z$ at spanwise positions $z/\lambda_z = \pm 0$ (triangles), $z/\lambda_z = \pm 1$ (circles), $z/\lambda_z = \pm 2$ (+), $z/\lambda_z = \pm 3$ (.), $z/\lambda_z = \pm 4$ ($*$), $z/\lambda_z = \pm 5$ (dash-dotted line), $z/\lambda_z = \pm 6$ (diamonds), $z/\lambda_z = \pm 7$ (dashed line) and time-averaged line (solid line).

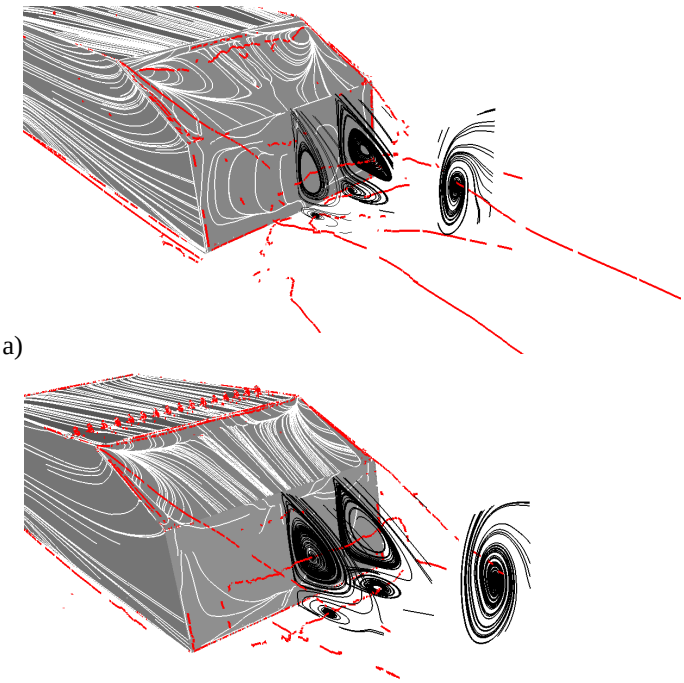

a)



b)

Fig. 14: Time-averaged flow structures around the rear of the body for a) natural flow and b) controlled flow. Vortex cores are shown in red (in the electronic version of the paper). Particle traces are shown in white on the vehicle. The streamlines are projected on two planes parallel with the symmetry plane of the body and one plane parallel with the vertical base of the body.

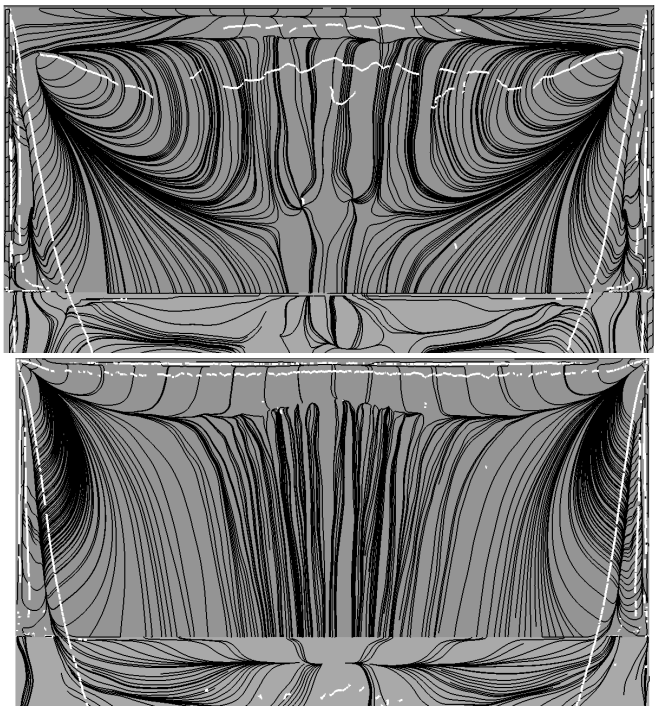


Fig. 15: Particle traces on the rear slanted surface from the present LES: a) natural flow and b) controlled flow.

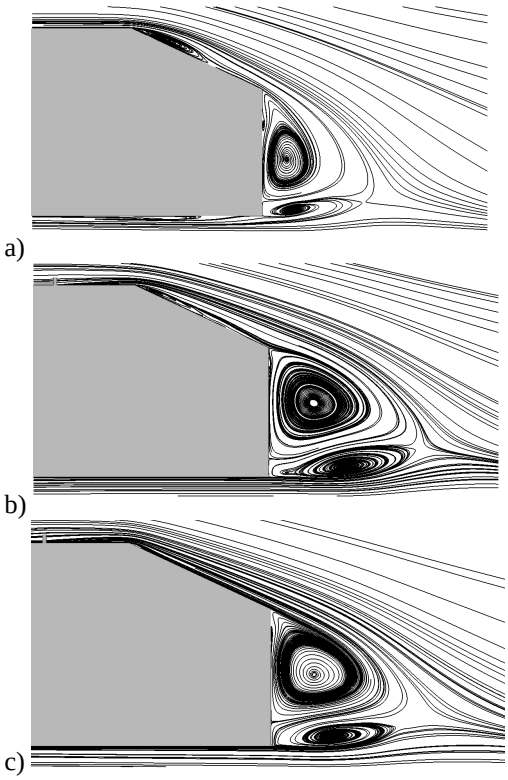


Fig. 16: Streamlines projected on the symmetry plane: a) natural flow, b) controlled flow (medium grid) and c) controlled flow (fine grid).

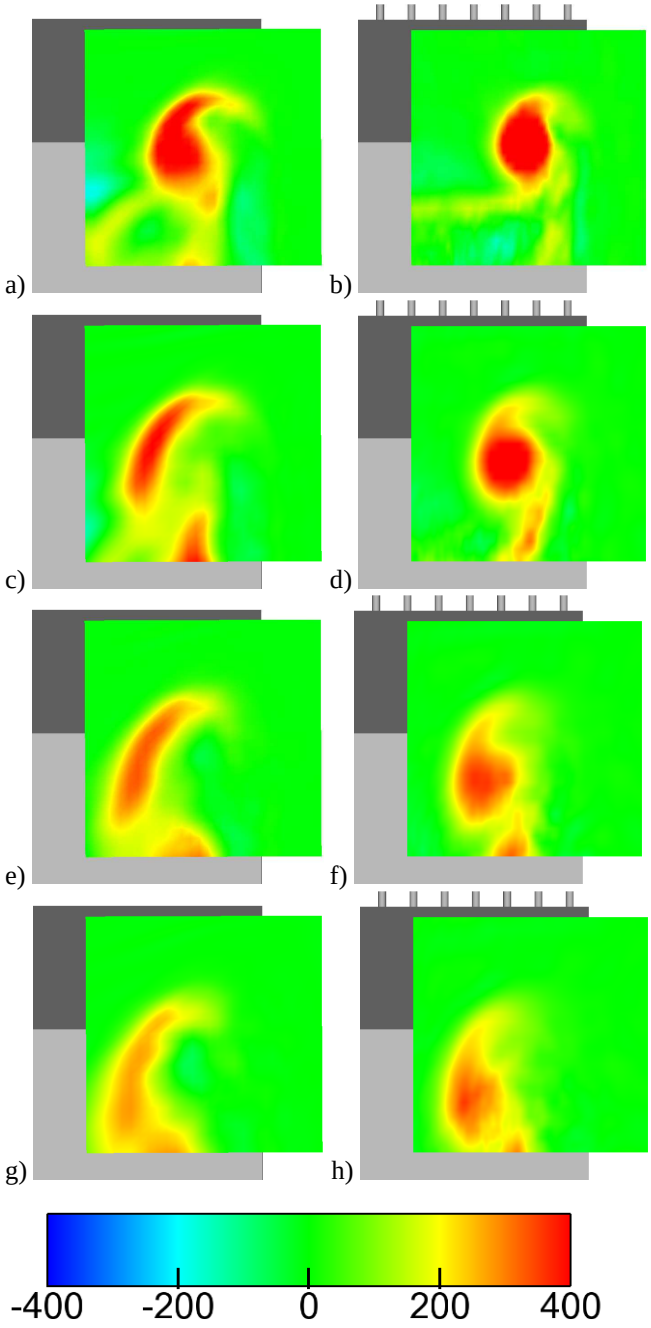


Fig. 17: Time-averaged vorticity component $\omega_x$ in planes a-b) 0.35 $H$, c-d) 0.52 $H$, e-f) 0.69 $H$ and g-h) 0.87 $H$.

a) 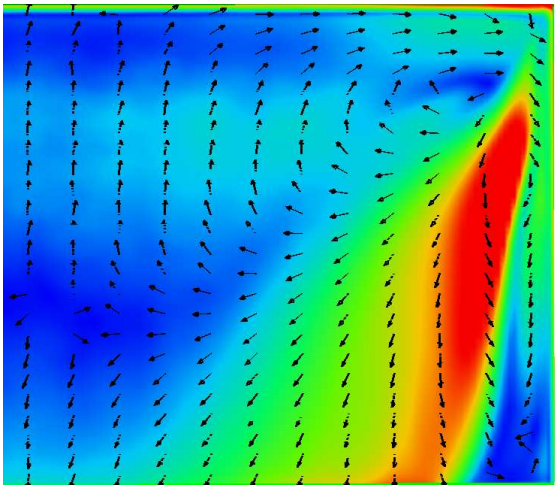 b) 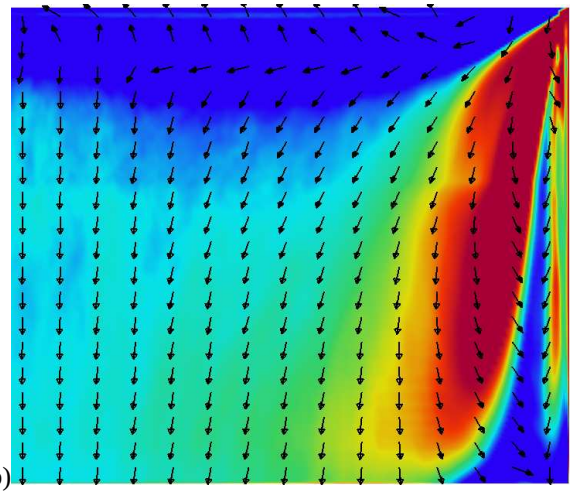

Fig. 18: Time-averaged streamline velocity in the plane parallel with the slanted surface at the constant distance $Y/k = 0.08$ above it. The flow is from top to bottom. The surface is colored with $U/U_\infty$. a) Natural flow (LES) and b) controlled flow (LES).

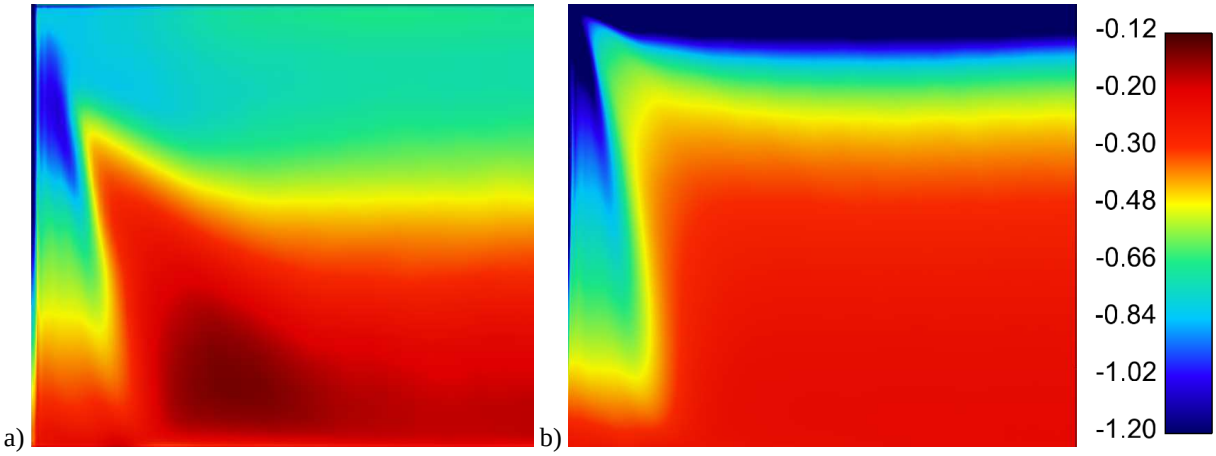


Fig. 19: Comparison of the surface pressure coefficient $C_p$ on the slanted surface of the model. a) Natural flow (LES) and b) controlled flow (LES).

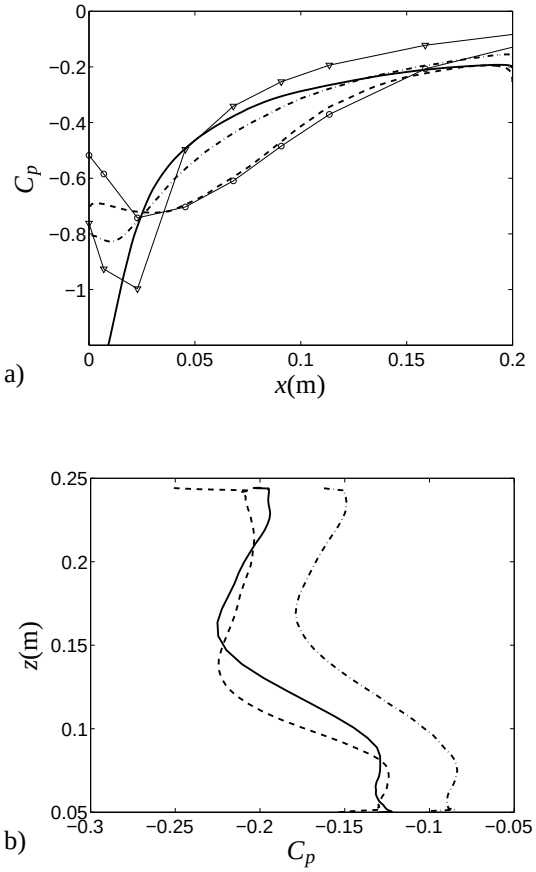


Fig. 20: Comparison of the surface pressure coefficient $C_p$ between the natural flow (dashed line) and the controlled flow (solid line) from fine grid LES on a) the slanted surface and b) the rear face of the body. The dash-dotted line is LES of the controlled flow using the medium grid. Experimental data for the natural and the controlled flows are plotted with circles and triangles, respectively. The profiles are shown for $y = 0$.